

Symmetry energy, neutron skin, and neutron star radius from chiral effective field theory interactions

K. Hebeler^{1,2} and A. Schwenk^{2,1}

¹ Institut für Kernphysik, Technische Universität Darmstadt, 64289 Darmstadt, Germany

² ExtreMe Matter Institute EMMI, GSI Helmholtzzentrum für Schwerionenforschung GmbH, 64291 Darmstadt, Germany

the date of receipt and acceptance should be inserted later

Abstract. We discuss neutron matter calculations based on chiral effective field theory interactions and their predictions for the symmetry energy, the neutron skin of ²⁰⁸Pb, and for the radius of neutron stars.

PACS. XX.XX.XX No PACS code given

1 Introduction

Chiral effective field theory (EFT) leads to a systematic expansion for nuclear forces [1, 2], as shown in Fig. 1, which provides a powerful approach to three-nucleon (3N) interactions [3] and enables controlled calculations with theoretical error estimates. This is especially important for exotic nuclei and neutron-rich matter under extreme conditions in astrophysics.

Neutron matter constitutes a unique system for chiral EFT, because all 3N and four-neutron (4N) interactions are predicted to next-to-next-to-next-to-leading order (N³LO) without free parameters [4, 5, 6]. In addition, neutron matter is a simpler system, in which one can test the chiral EFT power counting and the size of many-body forces for densities relevant to nuclei.

Generally, nuclear forces are not observable and depend on a resolution scale Λ , so that the nuclear Hamiltonian is given by

$$H(\Lambda) = T(\Lambda) + V_{\text{NN}}(\Lambda) + V_{\text{3N}}(\Lambda) + V_{\text{4N}}(\Lambda) \dots \quad (1)$$

As shown in Fig. 1, at a given order, nuclear forces include contributions from one- or multi-pion exchanges, which constitute the long-range parts, and from contact interactions, whose scale-dependent short-range couplings are fit to low-energy data for each Λ . There are natural sizes to many-body-force contributions that are made manifest in the EFT power counting and which explain the phenomenological hierarchy of many-body forces, $V_{\text{NN}}(\Lambda) > V_{\text{3N}}(\Lambda) > V_{\text{4N}}(\Lambda)$ [1].

The renormalization group (RG) is a powerful tool to systematically change the resolution scale Λ , while preserving low-energy observables. The evolution to lower scales facilitates the solution of the nuclear many-body problem due to a decoupling of low and high momenta in the Hamiltonian [7, 8]. In general, RG transformations change all terms of the Hamiltonian (1). Recently, it has

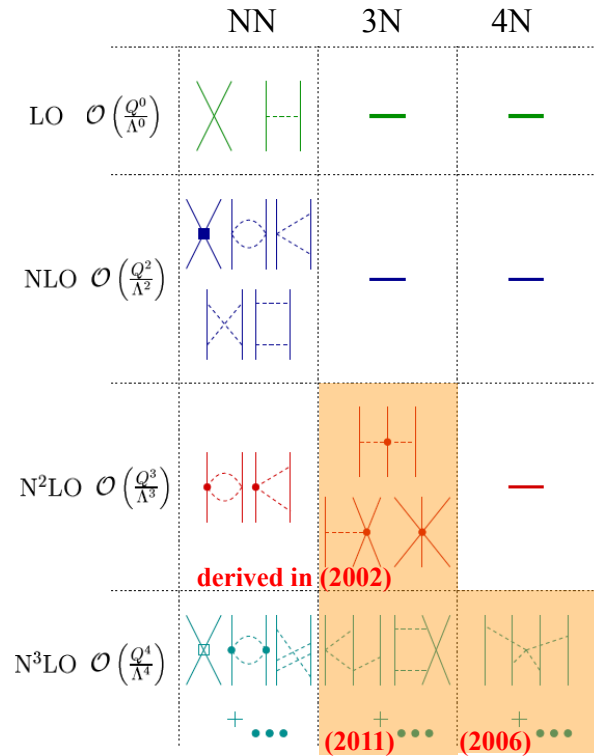


Fig. 1. Chiral EFT for nuclear forces, where the different contributions at successive orders are shown diagrammatically [1, 2]. Many-body forces are highlighted in orange including the year they were derived. All N³LO 3N and 4N forces are predicted parameter-free.

become possible to evolve 3N forces in momentum space [9], with first applications for neutron matter [10].

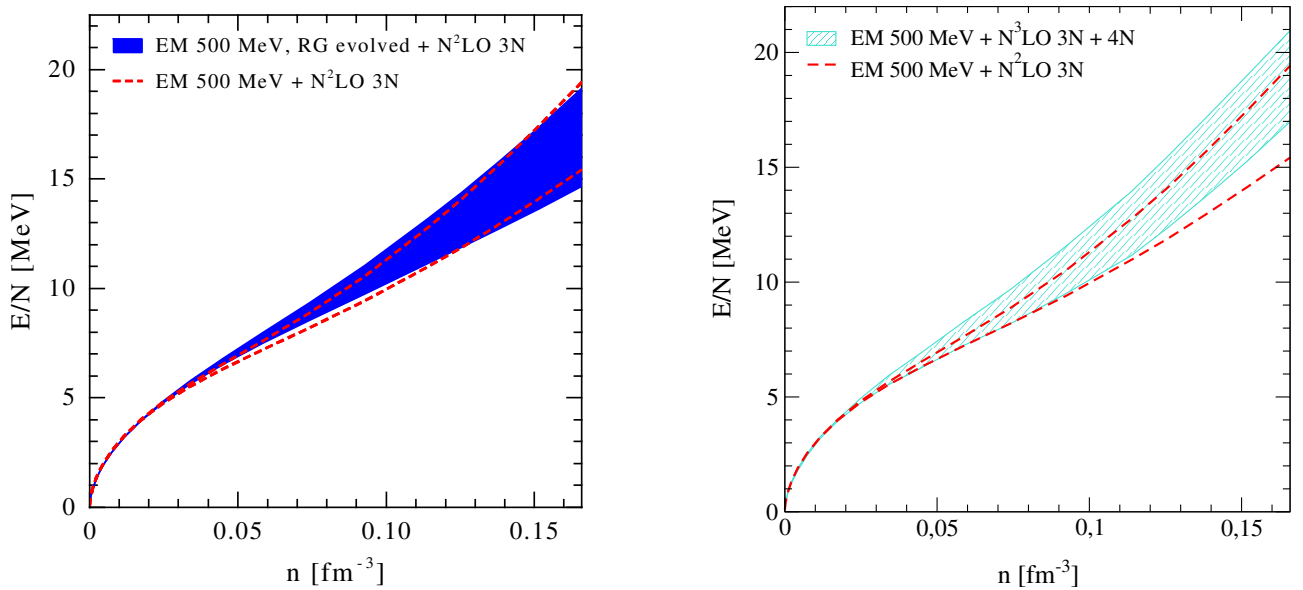


Fig. 2. Energy per particle E/N of neutron matter as a function of density n . The dashed red lines show the energy range [15] based on the EM 500 MeV N^3 LO NN potential of Ref. [14] including N^2 LO 3N interactions. The blue band in the left panel shows the corresponding results after RG-evolution of the NN potential [4,15]. The shaded cyan band in the right panel shows the results including all 3N and 4N contributions to N^3 LO (without RG evolution) [5,6].

2 Neutron matter based on chiral EFT interactions

At low resolution scales, the energy of nucleonic matter can be calculated with theoretical uncertainties in a perturbative expansion around the Hartree-Fock energy [4, 11,12,13]. Figure 2 shows the energy per particle of neutron matter up to saturation density $n_0 = 0.16 \text{ fm}^{-3}$. The results are based on the EM 500 MeV N^3 LO NN potential of Ref. [14]. The blue band in the left panel shows the energy per particle after RG-evolution of the NN potential to a low-momentum scale $\Lambda = 2.0 \text{ fm}^{-1}$ and including N^2 LO 3N interactions [4,15]. The same Hamiltonians fit only to light nuclei predict nuclear matter saturation with theoretical uncertainties [12]. At these scales, NN interactions derived from different NN potentials are very similar [16]. This universality can be attributed to the common long-range pion physics and the phase-shift equivalence of high-precision NN interactions. Consequently, the results for the energy per particle of neutron matter starting from different NN interactions are also very similar at these resolution scales. The width of the blue band is dominated by the uncertainties of the c_1 and c_3 couplings in 3N forces [4]. Because the leading chiral 3N forces are of long-range character in neutron matter, they are expected to be to a good approximation invariant under the RG evolution. Therefore, we use the N^2 LO 3N interactions determined by c_1 and c_3 also at low-resolution scales. As a comparison, the dashed red lines show the results based on the unevolved NN potential. The remarkable overlap indicates that neutron matter is, to a good approximation, perturbative for chiral NN interactions with $\Lambda \lesssim 500 \text{ MeV}$ (see Ref. [6] for details). This has been benchmarked by

first Quantum Monte Carlo (QMC) calculations with local chiral EFT interactions [17,18]. In addition, there are calculations of neutron matter using in-medium chiral perturbation theory approaches with similar results [19,20].

Figure 3 shows the first complete N^3 LO calculation of the neutron matter energy, which includes all NN, 3N and 4N interactions to N^3 LO [5,6]. The energy range is based on different NN potentials, a variation of the couplings $c_1 = -(0.75-1.13) \text{ GeV}^{-1}$, $c_3 = -(4.77-5.51) \text{ GeV}^{-1}$ [21], which dominates the total uncertainty, a 3N/4N-cutoff variation $\Lambda = 2 - 2.5 \text{ fm}^{-1}$, and the uncertainty in the many-body calculation. The N^3 LO range is in very good agreement with NLO lattice results [22] and QMC simulations [23] at very low densities (see also the inset), where the properties are determined by the large scattering length and effective range [24]. We also find a very good agreement with other ab initio calculations of neutron matter based on the Argonne NN and Urbana 3N potentials: In Fig. 3, we compare our N^3 LO results with variational calculations (APR) [25], which are within the N^3 LO band, but do not provide theoretical uncertainties. In addition, we compare the density dependence with results from Auxiliary Field Diffusion MC (AFDMC) calculations (GCR) [26] based on nuclear force models adjusted to an energy difference of 32 MeV between neutron matter and the empirical saturation point.

In the right panel of Fig. 2, we compare the N^3 LO energy obtained from the EM 500 MeV N^3 LO NN potential to the results that include only N^2 LO 3N interactions (dashed red lines). Note that it will be important to study the EFT convergence of 3N forces from N^2 LO to N^3 LO in more detail, as we find relatively large individual 3N contributions at N^3 LO (see Refs. [5,6] for details), and also

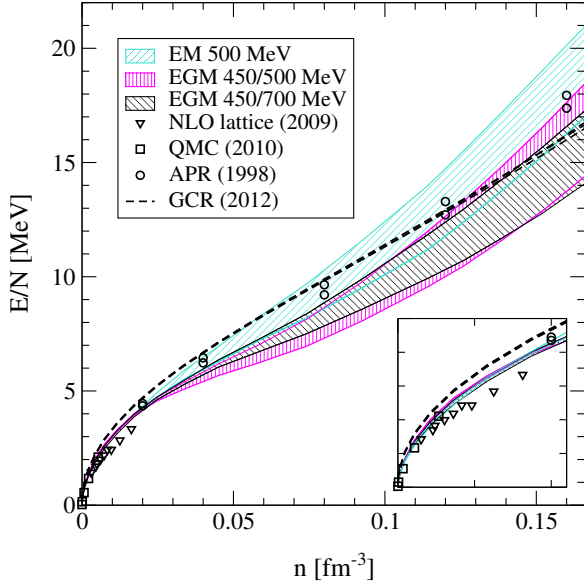


Fig. 3. Neutron matter energy per particle as a function of density including NN, 3N and 4N forces at $N^3\text{LO}$. The three overlapping bands are labeled by the different NN potentials and include uncertainty estimates due to the many-body calculation, the low-energy c_i constants, and by varying the 3N/4N cutoffs (see Refs. [5,6] for details). For comparison, results are shown at low densities (see also the inset) from NLO lattice [22] and Quantum Monte Carlo (QMC) simulations [23], and at nuclear densities from variational (APR) [25] and Auxiliary Field Diffusion MC calculations (GCR) [26] based on 3N potentials adjusted to nuclear matter properties.

the low-energy couplings c_i in NN and 3N interactions depend on the chiral order [21]. As a result, the width of the energy bands based on 3N forces at $N^2\text{LO}$ and $N^3\text{LO}$ are comparable at higher densities.

3 From the neutron matter equation of state to the symmetry energy and neutron skin

We extend our ab initio results for neutron matter to matter with a finite proton fraction $x = n_p/n$ by using an empirical parametrization [15] of the energy per particle E/A that includes kinetic energy plus interaction energy, which is expanded in the Fermi momentum and is quadratic in the neutron excess $1 - 2x$,

$$\frac{E/A(\bar{n}, x)}{T_0} = \frac{3}{5} \left[x^{5/3} + (1-x)^{5/3} \right] (2\bar{n})^{2/3} - [(2\alpha - 4\alpha_L)x(1-x) + \alpha_L] \bar{n} + [(2\eta - 4\eta_L)x(1-x) + \eta_L] \bar{n}^{4/3}. \quad (2)$$

Here $\bar{n} = n/n_0$ is the baryon density in units of the saturation density and $T_0 = (3\pi^2 n_0/2)^{2/3} \hbar^2/(2m) = 36.84$ MeV is the Fermi energy of symmetric nuclear matter at saturation density. The corresponding expression for the pressure follows from $P = n^2 \partial(E/A)/\partial n$. The empirical parametrization interpolates between the properties of neutron

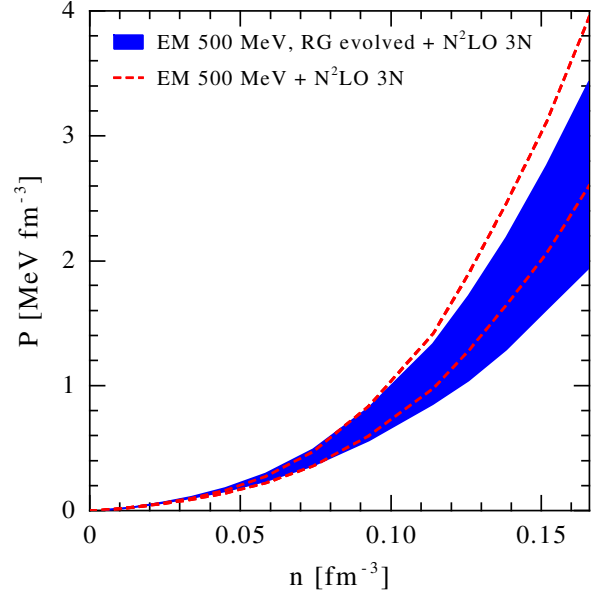


Fig. 4. Pressure P of neutron matter as a function of density n . Results are shown for the same NN and 3N interactions as for the energy in the left panel of Fig. 2.

matter and symmetric matter and was recently benchmarked against ab initio calculations of asymmetric matter with very good agreement [13].

The parameters α, η and α_L, η_L can be determined from the empirical saturation properties of symmetric matter ($x = 1/2$) and from the microscopic calculations of neutron matter ($x = 0$), respectively. The empirical saturation point $E/A(\bar{n} = 1, x = 1/2) = -16$ MeV and $P(\bar{n} = 1, x = 1/2) = 0$ gives $\alpha = 5.87$, $\eta = 3.81$ with a reasonable incompressibility $K = 236$ MeV, where the precise value of K could be adjusted by modifying the exponent $4/3$ in the parametrization (2). However, the predicted range for the symmetry energy and its density derivative depend very weakly on this choice [15].

The parameters α_L, η_L are extracted from the calculated bands for the neutron matter energy and pressure. For this, we use the results based on RG-evolved NN interactions, given by the blue bands in Fig. 2 for the energy and Fig. 4 for the pressure. Due to the improved convergence by the RG, the uncertainties from the many-body calculation are smaller than for unevolved interactions. To determine α_L, η_L , we sample their values and require that the resulting energy and pressure are within the uncertainty bands (see Ref. [15] for details).

The parametrization (2) allows to predict the symmetry energy S_v and its density derivative L ,

$$S_v = \frac{1}{8} \left. \frac{\partial^2 \epsilon(\bar{n}, x)}{\partial x^2} \right|_{\bar{n}=1, x=1/2} \quad (3)$$

$$L = \frac{3}{8} \left. \frac{\partial^3 \epsilon(\bar{n}, x)}{\partial \bar{n} \partial x^2} \right|_{\bar{n}=1, x=1/2}. \quad (4)$$

The values for α_L, η_L translate into correlated ranges for $S_v = 29.7 - 33.2$ MeV and $L = 32.5 - 57.0$ MeV [15].

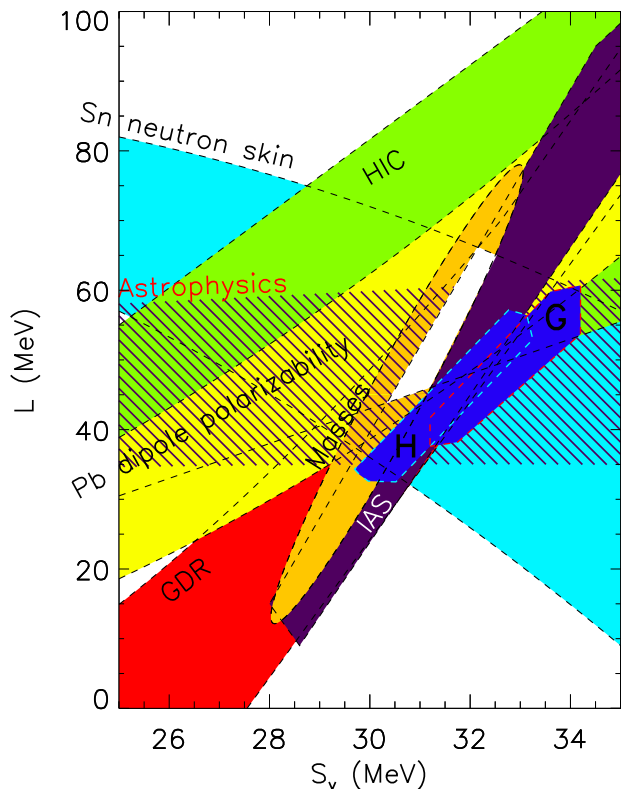


Fig. 5. Constraints for the symmetry energy S_v and the L parameter following [27]. The blue region labeled “H” shows our neutron matter constraints, “G” represents the results of Ref. [26] adjusted to a range of the symmetry energy. These are compared to bands based on different empirical extractions (for details see Refs. [15, 28]). The white area gives the overlap region of the different empirical ranges.

In Fig. 5, we compare the $S_v - L$ region predicted by our neutron matter results with bands extracted from other analyses [15, 27, 28]. Strikingly, the neutron matter results provide the tightest constraints. They agree well with constraints obtained from energy-density functionals for nuclear masses (orange band) [28, 29] as well as from the ^{208}Pb dipole polarizability (yellow band) [28, 30, 31, 32] and from a recent analysis of isobaric analog states (IAS, purple band) [33]. In addition, there is good agreement with studies of the Sn neutron skin (light blue band) [34], of isotope diffusion in heavy ion collisions (HIC, green band) [35], and of giant dipole resonances (GDR, red band) [36]. For additional details see Refs. [27, 28]. Moreover, there is very good agreement with an estimate obtained from modeling X-ray bursts and quiescent low-mass X-ray binaries (“Astrophysics”, shaded region) [37].

It is also remarkable how well the $S_v - L$ region predicted by our neutron matter results agrees with the one obtained from the AFDMC calculations [26] based on a set of very different Hamiltonians, the Argonne v'_8 NN and Urbana IX 3N potentials (“G” in Fig. 5), where the region is constructed from different 3N models with a symmetry energy between the NN only and NN plus Urbana IX 3N

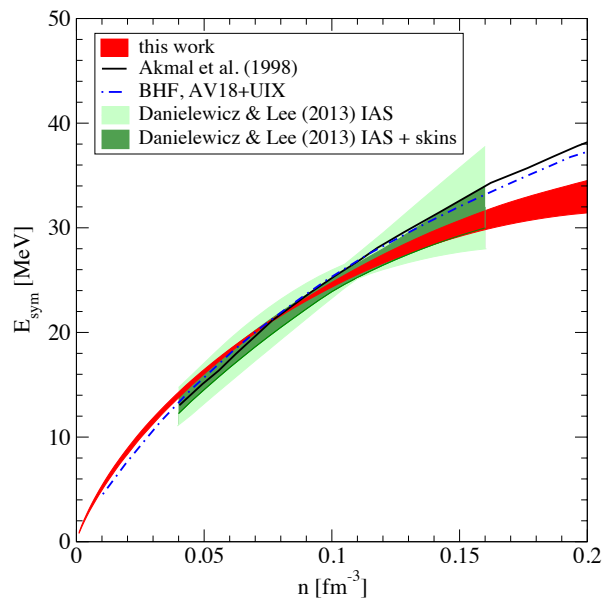


Fig. 6. E_{sym} as a function of density obtained from ab initio calculations of asymmetric matter [13]. In comparison, we give E_{sym} obtained from microscopic calculations performed with a variational approach (Akmal et al. (1998)) [25] and at the Brueckner-Hartree-Fock level (BHF) [38] based on the Argonne v_{18} NN and Urbana UIX 3N potentials (with parameters adjusted to the empirical saturation point). The band over the density range $n = 0.04 - 0.16 \text{ fm}^{-3}$ is based on a recent analysis of isobaric analog states (IAS) and including the constraints from neutron skins (IAS + skins) [33].

result (an intermediate model in this set is given by the GCR curve in Fig. 3).

Recently, the symmetry energy was studied in ab initio calculations of asymmetric matter based on N^3LO NN and N^2LO 3N interactions [13]. The energy of asymmetric matter was found to compare very well with a quadratic expansion even for neutron-rich conditions, which was then used to extract the quadratic symmetry-energy term E_{sym} . In contrast to other calculations, the results are based on 3N forces fit only to light nuclei, without adjustments to empirical nuclear matter properties. The results for E_{sym} are compared in Fig. 6 with constraints from a recent analysis of isobaric analog states (IAS) and including the constraints from neutron skins (IAS + skins) [33], showing a remarkable agreement over the entire density range. Note that compared to extracting the symmetry energy from neutron matter calculations using the parametrization (2), the uncertainty is reduced due to the explicit information from asymmetric matter.

The neutron skin probes the properties of neutron matter, as a higher pressure at typical nuclear densities implies larger neutron skins [39]. Using these correlations [39] (and including a study based on the liquid droplet model), our neutron matter results of the blue bands in Figs. 2 and 4 predict the neutron skin of ^{208}Pb to $0.17 \pm 0.03 \text{ fm}$ [40], which is in excellent agreement with the extraction of $0.156^{+0.025}_{-0.021} \text{ fm}$ from the dipole polarizability [30]. The the-

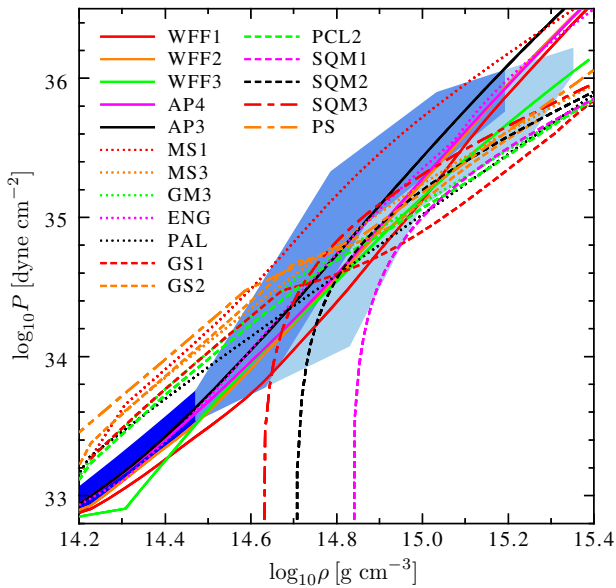


Fig. 7. Constraints for the pressure P of neutron star matter as a function of mass density ρ compared to EOSs commonly used to model neutron stars [45]. The lighter blue band is the envelope of the general polytropic extensions that are causal and support a neutron star of mass $\widehat{M} = 1.97 M_{\odot}$ and the darker blue band at high densities corresponds to $\widehat{M} = 2.4 M_{\odot}$ [15].

oretical uncertainty is also smaller than the target goal of a new PREX measurement using parity violating electron scattering at JLAB [41]. Moreover, including properties of doubly-magic nuclei as constraints, in addition to low-density neutron matter results, leads to even tighter predictions for the neutron skins of ^{208}Pb and ^{48}Ca to be 0.182 ± 0.010 fm and 0.173 ± 0.005 fm, respectively [42].

4 Constraints on neutron star radii

We also use the parametrization (2) to extend the neutron matter results to neutron star matter in beta equilibrium. The proton fraction in beta equilibrium is determined by minimizing the total energy per particle with respect to x at a given density including the contributions from electrons and from the rest mass of the nucleons,

$$\frac{\partial E/A(\bar{n}, x)}{\partial x} + \mu_e(\bar{n}, x) - (m_n - m_p)c^2 = 0. \quad (5)$$

Based on the neutron matter bands, this leads to a proton fraction of 4% – 5.3% at saturation density and a crust-core transition density at $n \approx n_0/2$ [15]. To describe the equation of state (EOS) of neutron star matter, we use the BPS outer crust EOS for densities below $n_0/2$ [43, 44]. Note that without 3N forces, the calculated EOSs would not match on to a standard crust EOS [40].

Because the central densities of neutron stars can significantly exceed the regime of our neutron matter calculations, we extend the EOSs for $n > 1.1 n_0$ by employing

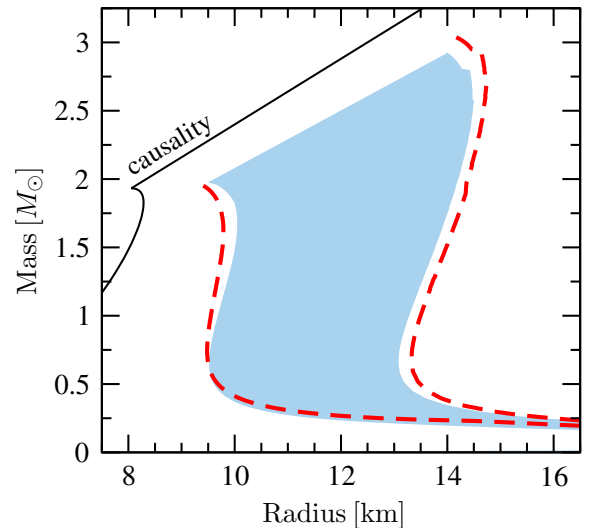


Fig. 8. Neutron star mass-radius constraints based on the uncertainty band for the EOSs of Fig. 7 for $\widehat{M} = 1.97 M_{\odot}$. The blue region gives the radius constraints based on the neutron matter results with RG-evolved interactions, the red dashed lines based on unevolved interactions, as in the left panel of Fig. 2.

general piecewise polytropic extensions [40, 15]. This strategy generates a very large number of EOSs, allows for soft regions and constitutes a complete set of possible EOSs at high densities, independent of the assumptions on the interactions and constituents of matter at high densities. We solve the Tolman-Oppenheimer-Volkov equations for each of these EOSs and retain only those that 1) remain causal for all relevant densities, and 2) are able to support a neutron star mass $M = \widehat{M}$, the mass of the heaviest neutron star observed or potential heavier candidates.

In Fig. 7, we compare the resulting EOS uncertainty bands with a representative set of EOSs used in the literature [45]. The low-density pressure sets the scale, and then the lighter blue band correspond to the mass constraint $\widehat{M} = 1.97 M_{\odot}$, the central value of the two-solar-mass neutron star measured by Shapiro delay [46] and the lower 1σ mass of the recently observed most massive neutron star from radio timing observations [47], whereas the darker blue band corresponds to $\widehat{M} = 2.4 M_{\odot}$, a fictitious heavier neutron star. Figure 7 demonstrates that chiral EFT interactions provide strong constraints, ruling out many model EOSs at low densities and, combined with the astrophysics constraint of a heavy neutron star, at high densities as well. Table 1 shows that these constraints imply that a 1.4 (1.97) M_{\odot} neutron star does not exceed densities beyond 4.4 (7.6) n_0 , which corresponds to a Fermi momentum of only 550 (660) MeV.

From the EOS uncertainty bands in Fig. 7 we can directly derive constraints for the radii of neutron stars. In Fig. 8, we present the radius constraints obtained from the EOS band of Fig. 7 for $\widehat{M} = 1.97 M_{\odot}$. We calculated the mass-radius relationships for the individual EOSs by solv-

| | $\widehat{M} = 1.97 M_{\odot}$ | | $\widehat{M} = 2.4 M_{\odot}$ | |
|--------------------------------------|--------------------------------|-----|-------------------------------|-----|
| | min | max | min | max |
| ρ_c/ρ_0 ($1.4 M_{\odot}$) | 1.8 | 4.4 | 1.8 | 2.7 |
| ρ_c/ρ_0 ($1.97 M_{\odot}$) | 2.0 | 7.6 | 2.0 | 3.4 |
| ρ_c/ρ_0 ($2.4 M_{\odot}$) | | | 2.2 | 5.4 |

Table 1. Minimal and maximal central densities ρ_c (in units of the saturation density ρ_0).

ing the Tolman-Oppenheimer-Volkov equations. Based on all these results we constructed an envelope based on the extreme values (see Ref. [15] for details). The blue region (red dashed lines) in Fig. 8 show the radius constraints based on the neutron matter results with RG-evolved (un-evolved) interactions, as in the left panel of Fig. 2. For a typical $1.4 M_{\odot}$ neutron star, we predict a radius range of $R = 9.7 - 13.9$ km. Our radius range is also consistent with astrophysical extractions obtained from modeling X-ray burst sources (see, e.g., Ref. [37]), and the neutron matter constraints have recently been explored for the gravitational wave signal in neutron-star mergers [48]. Finally, all EOSs for cold matter in beta equilibrium should go through the EOS uncertainty bands, independent of composition, and we have constructed three representative EOSs for astrophysical applications [15].

5 Summary and outlook

We have shown that the properties of neutron-rich matter at nuclear densities are well constrained by chiral EFT interactions. This results in tight constraints for the symmetry energy, the neutron skin of ^{208}Pb , and for the radius of neutron stars. The theoretical uncertainties are dominated by the uncertainties in 3N forces. Therefore, developments in 3N forces will be important next steps for nuclei and nucleonic matter. These include their consistent SRG evolution, improved treatments with $N^3\text{LO}$ interactions, and by going to a Delta-full EFT.

Neutron-rich matter is also the focus of rare isotope beam facilities worldwide, where predictions based on the same nuclear forces can be tested in exotic nuclei. This goes hand in hand with advances in many-body methods and studying 3N forces in medium-mass neutron-rich nuclei, where the frontier of ab initio calculations is presently in the calcium region [49, 50, 51, 52, 53, 54, 55]. This promises further interesting developments from ab initio calculations for the neutron skin of ^{48}Ca .

Acknowledgements

We would like to thank C. Drischler, T. Krüger, J. M. Lattimer, C. J. Pethick, V. Somà, and I. Tews, who contributed to the results discussed in this short topical review. This work was supported by the DFG through Grant SFB 634, by the ERC Grant No. 307986 STRONGINT, and by the Helmholtz Alliance HA216/EMMI.

References

1. E. Epelbaum, H.-W. Hammer, and U.-G. Meißner, *Rev. Mod. Phys.* **81**, 1773 (2009).
2. R. Machleidt and D. R. Entem, *Phys. Rept.* **503**, 1 (2011).
3. H.-W. Hammer, A. Nogga, and A. Schwenk, *Rev. Mod. Phys.* **85**, 197 (2013).
4. K. Hebeler and A. Schwenk, *Phys. Rev. C* **82**, 014314 (2010).
5. I. Tews, T. Krüger, K. Hebeler, and A. Schwenk, *Phys. Rev. Lett.* **110**, 032504 (2013).
6. T. Krüger, I. Tews, K. Hebeler, and A. Schwenk, *Phys. Rev. C* **88**, 025802 (2013).
7. S. K. Bogner, R. J. Furnstahl, and A. Schwenk, *Prog. Part. Nucl. Phys.* **65**, 94 (2010).
8. R. J. Furnstahl and K. Hebeler, *Rep. Prog. Phys.* **76**, 126301 (2013).
9. K. Hebeler, *Phys. Rev. C* **85**, 021002(R) (2012).
10. K. Hebeler and R. J. Furnstahl, *Phys. Rev. C* **87**, 031302(R) (2013).
11. S. K. Bogner, A. Schwenk, R. J. Furnstahl, and A. Nogga, *Nucl. Phys. A* **763**, 59 (2005).
12. K. Hebeler, S. K. Bogner, R. J. Furnstahl, A. Nogga, and A. Schwenk, *Phys. Rev. C* **83**, 031301(R) (2011).
13. C. Drischler, V. Somà, and A. Schwenk, *Phys. Rev. C* in press, arXiv:1310.5627.
14. D. R. Entem and R. Machleidt, *Phys. Rev. C* **68**, 041001(R) (2003).
15. K. Hebeler, J. M. Lattimer, C. J. Pethick, and A. Schwenk, *Astrophys. J.* **773**, 11 (2013).
16. S. K. Bogner, T. T. S. Kuo, and A. Schwenk, *Phys. Rept.* **386**, 1 (2003).
17. A. Gezerlis, I. Tews, E. Epelbaum, S. Gandolfi, K. Hebeler, A. Nogga, and A. Schwenk, *Phys. Rev. Lett.* **111**, 032501 (2013).
18. I. Tews, T. Krüger, A. Gezerlis, K. Hebeler, and A. Schwenk, arXiv:1310.3643.
19. N. Kaiser, S. Fritsch, and W. Weise, *Nucl. Phys. A* **697**, 255 (2002); J. W. Holt, N. Kaiser, and W. Weise, *Prog. Part. Nucl. Phys.* **73**, 35 (2013).
20. A. Lacour, J. A. Oller, and U.-G. Meißner, *Annals Phys.* **326**, 241 (2011).
21. H. Krebs, A. Gasparyan, and E. Epelbaum, *Phys. Rev. C* **85**, 054006 (2012).
22. E. Epelbaum, H. Krebs, D. Lee, and U.-G. Meißner, *Eur. Phys. J. A* **40**, 199 (2009).
23. A. Gezerlis and J. Carlson, *Phys. Rev. C* **81**, 025803 (2010); A. Gezerlis and R. Sharma, *Phys. Rev. C* **85**, 015806 (2012).
24. A. Schwenk and C. J. Pethick, *Phys. Rev. Lett.* **95**, 160401 (2005).
25. A. Akmal, V. R. Pandharipande, and D. G. Ravenhall, *Phys. Rev. C* **58**, 1804 (1998).
26. S. Gandolfi, J. Carlson, and S. Reddy, *Phys. Rev. C* **85**, 032801(R) (2012); S. Gandolfi, J. Carlson, S. Reddy, A. W. Steiner, and R. B. Wiringa, this volume, arXiv:1307.5815.
27. J. M. Lattimer and Y. Lim, *Astrophys. J.* **771**, 51 (2013).
28. J. M. Lattimer and A. W. Steiner, this volume.
29. M. Kortelainen, T. Lesinski, J. Moré, W. Nazarewicz, J. Sarich, N. Schunck, M. Stoitsov, and S. Wild, *Phys. Rev. C* **82**, 024313 (2010).
30. A. Tamii *et al.*, *Phys. Rev. Lett.* **107**, 062502 (2011).

31. A. Tamii, P. von Neumann-Cosel, and I. Poltoratska, this volume, arXiv:1307.2706.
32. W. Nazarewicz, P.G. Reinhard, W. Satula, and D. Vretenar, this volume, arXiv:1307.5782.
33. P. Danielewicz and J. Lee, Nucl. Phys. A **922**, 1 (2014).
34. L.-W. Chen, C. M. Ko, B.-A. Li, and J. Xu, Phys. Rev. C **82**, 024321 (2010).
35. M. B. Tsang *et al.*, Phys. Rev. Lett. **102**, 122701 (2009).
36. L. Trippa, G. Colò, and E. Vigezzi, Phys. Rev. C **77**, 061304 (2008).
37. A. W. Steiner, J. M. Lattimer, and E. F. Brown, Astrophys. J. **722**, 33 (2010); Astrophys. J. **765**, L5 (2013).
38. G. Taranto, M. Baldo and G. F. Burgio, Phys. Rev. C **87**, 045803 (2013).
39. B. A. Brown, Phys. Rev. Lett. **85**, 5296 (2000); S. Typel and B. A. Brown, Phys. Rev. C **64**, 027302 (2001).
40. K. Hebeler, J. M. Lattimer, C. J. Pethick, and A. Schwenk, Phys. Rev. Lett. **105**, 161102 (2010).
41. S. Abrahamyan *et al.*, Phys. Rev. Lett. **108**, 112502 (2012).
42. B. A. Brown and A. Schwenk, Phys. Rev. C rapid comm. in press, arXiv:1311.3957.
43. G. Baym, C. J. Pethick, and P. Sutherland, Astrophys. J. **170**, 299 (1971).
44. J. W. Negele and D. Vautherin, Nucl. Phys. A **207**, 298 (1973).
45. J. M. Lattimer and M. Prakash, Astrophys. J. **550**, 426 (2001).
46. P. B. Demorest, T. Pennucci, S. M. Ransom, M. S. E. Roberts, and J. W. T. Hessels, Nature **467**, 1081 (2010).
47. J. Antoniadis *et al.*, Science **340**, 448 (2013).
48. A. Bauswein and H.-T. Janka, Phys. Rev. Lett. **108**, 011101 (2012); A. Bauswein, H.-T. Janka, K. Hebeler, and A. Schwenk, Phys. Rev. D **86**, 063001 (2012).
49. J. D. Holt, T. Otsuka, A. Schwenk, and T. Suzuki, J. Phys. G **39**, 085111 (2012).
50. G. Hagen, M. Hjorth-Jensen, G. R. Jansen, R. Machleidt, and T. Papenbrock, Phys. Rev. Lett. **109**, 032502 (2012).
51. R. Roth, S. Binder, K. Vobig, A. Calci, J. Langhammer, and P. Návratil, Phys. Rev. Lett. **109**, 052501 (2012).
52. A. T. Gallant *et al.*, Phys. Rev. Lett. **109**, 032506 (2012).
53. J. D. Holt, J. Menéndez, and A. Schwenk, J. Phys. G **40**, 075105 (2013).
54. F. Wienholtz *et al.*, Nature **498**, 346 (2013).
55. V. Somà, A. Cipollone, C. Barbieri, P. Navrátil, and T. Duguet, arXiv:1312.2068.